Research Article

Journal of Environmental Nanotechnology

Green Synthesis, Characterization, and Visible-light Photocatalytic Application of Mo–TiO_2 for Reactive Orange 16 Degradation: RSM Optimization and GPR Modeling

Arumugam Gopal[1*], J. Saravanan[2], Anand M Raikar[3] and L. Muthulakshmi[4]

[1]Department of Chemical Engineering, Vel Tech High Tech Dr.Rangarajan Dr.Sakunthala Engineering College, Avadi, Chennai, TN, India
[2]Department of Chemical Engineering, Mohamed Sathak Engineering College, Kilakarai, Ramanathapuram, TN, India
[3]Department of Aerospace Engineering, Ramaiah Institute of Technology, Bengaluru, KA, India
[4]Department of Master of Computer Applications, M. Kumarasamy College of Engineering (Autonomous), Karur, TN, India
Received: 28.07.2026 Accepted: 27.08.2026 Published: 30.09.2026
*arumugamchem1979@gmail.com

ABSTRACT

The present study developed a green-synthesized molybdenum-doped titanium dioxide (Mo–TiO_2) photocatalyst using pomegranate peel extract and evaluated its performance for the degradation of Reactive Orange 16 (RO16) under visible-light irradiation. The effects of pH, catalyst dosage, initial RO16 concentration, and irradiation time were investigated using a four-factor Box–Behnken design comprising 27 experimental runs. The resulting quadratic model was statistically significant ($p < 0.0001$), with $R^2 = 0.9996$, adjusted $R^2 = 0.9992$, predicted $R^2 = 0.9979$, and a nonsignificant lack of fit ($p = 0.3631$). Numerical optimization predicted 96.27% RO16 decolourization at pH 7.07, a catalyst dosage of 50.40 mg L^{-1}, an initial RO16 concentration of 17.75 mg L^{-1}, and an irradiation time of 68.12 min. Experimental confirmation yielded 95.88% decolorization, corresponding to an RSM prediction error of approximately 0.40%. For exploratory machine-learning modelling, the 27-run experimental dataset was computationally augmented to 120 observations and evaluated using Gaussian Process Regression (GPR), Support Vector Regression, Gradient Boosting, multilayer perceptron artificial neural network, and Bagged Random Trees. Among the five evaluated models, GPR showed the best performance within the augmented dataset, achieving a test R^2 of 0.99390 and a five-fold cross-validated R^2 of 0.99098. These metrics represent internal computational validation and should not be interpreted as independent experimental validation. Under the optimized conditions, GPR predicted 96.31% RO16 decolourization, closely agreeing with the RSM prediction. Permutation analysis identified the initial RO16 concentration as the most influential predictor, followed by catalyst dosage, irradiation time, and pH. Overall, the integration of green synthesis, RSM optimization, and GPR modelling provides a promising framework for modelling and optimizing photocatalytic treatment of dye-contaminated water.

Keywords: Reactive orange 16; Mo-doped TiO_2; Photocatalytic degradation; Response surface methodology; Gaussian process regression; Green synthesis.

1. INTRODUCTION

Rapid expansion of the dyeing, textile, printing, and chemical industries has resulted in the continuous discharge of hazardous organic pollutants into aquatic environments. Among the contaminants, azo dyes such as Reactive Orange 16 (RO16) were of particular concern due to their complex aromatic structures, high chemical stability, and resistance to biological degradation. RO16 is particularly relevant because its azo-linked aromatic structure, strong coloration, and chemical persistence hinder conventional biological treatment and light penetration in contaminated water. Its occurrence in textile wastewater and potential formation of hazardous transformation products therefore make RO16 an appropriate model pollutant for evaluating visible-light photocatalytic treatment. The persistence of dyes reduces light penetration in water bodies, inhibits photosynthetic activity, and generates toxic or carcinogenic intermediates that threaten both aquatic ecosystems and human health. The degradation of azo dyes may generate aromatic amines and other transformation products with potential toxic, mutagenic, or carcinogenic effects, emphasizing the need to evaluate degradation products in addition to colour removal (Golka *et al.* 2004). Consequently, improvement of sustainable, efficient, and environmentally benign technology for dye removal has become an important research priority. Among various wastewater treatment technologies, semiconductor photocatalysis has emerged as one of the most promising advanced oxidation processes because it enables the mineralization of organic pollutants into harmless products under light irradiation. Titanium dioxide (TiO_2) has been widely investigated as an environmentally

benign photocatalytic material because of its non-toxicity, chemical stability, and compatibility with low-cost green-synthesis routes. The practical application of pristine TiO_2 was limited by its wide band gap, rapid recombination of photogenerated electron-hole pairs, and limited utilization of visible light.

In particular, Mo-modified TiO_2 has attracted considerable attention because Mo ions introduce intermediate energy levels within the TiO_2 lattice, facilitating efficient electron transport and prolonged charge separation. Mo species can generate localized donor/trap states and oxygen-vacancy-related defects within TiO_2, thereby reducing the effective excitation-energy requirement and extending photoresponse toward visible wavelengths. These defect states can temporarily trap photogenerated electrons, suppress rapid electron–hole recombination, and promote interfacial formation of reactive oxygen species, thereby improving visible-light photocatalytic activity. CTAB-modified Mo-doped TiO_2/fly ash cenosphere photocatalysts prepared by the sol-gel method achieved 99.75% methylene blue degradation within 60 min owing to broadened visible-light absorption and abundant oxygen vacancies (Li *et al.* 2022). Likewise, vermiwash-assisted, green-synthesized Mo-doped TiO_2 nanoparticles enhanced methylene blue degradation from 73% to 97% while simultaneously exhibiting antibacterial, antioxidant, and antidiabetic activities, thereby demonstrating the multifunctionality of bio-mediated photocatalysts (Ravichandran *et al.* 2024). Furthermore, Mo-doped TiO_2 supported on granular activated carbon exhibited remarkable degradation of volatile organic compounds under both UV and visible light due to its improved crystallinity and enhanced charge-transfer characteristics (Abedi *et al.* 2022). Although these studies confirm the beneficial photocatalytic effects of Mo modification, they employ different synthesis routes, supports, and target pollutants, particularly methylene blue and volatile organic compounds. Green synthesis specifically targeting RO16, systematic multivariable optimization, predictive modelling, long-term catalyst stability, and scale-up considerations remain comparatively less explored. The present work addresses the synthesis–RO16–optimization–modelling gap, while recyclability and scale-up require further validation. Beyond photocatalysis, Mo-doped TiO_2 nanostructures have also demonstrated excellent gas-sensing performance owing to their high surface area and mesoporous morphology (Setiye *et al.* 2025).

Recently, green synthesis has emerged as an environmentally sustainable alternative to conventional chemical synthesis, replacing hazardous reducing agents with naturally occurring phytochemicals found in plant extracts. Plant-derived biomolecules such as flavonoids, polyphenols, tannins, and organic acids serve as reducing, stabilizing, and capping agents, enabling the synthesis of nanomaterials under mild reaction conditions while minimizing environmental impacts. Pomegranate peel is an abundant agricultural waste rich in antioxidant phytochemicals that can facilitate nanoparticle synthesis. Its polyphenols, flavonoids, tannins, and organic acids contain hydroxyl and carbonyl functionalities capable of interacting with Ti and Mo precursor species. These phytochemicals can function as complexing and stabilizing agents during precursor hydrolysis, moderating nucleation, particle growth, and excessive agglomeration while simultaneously valorizing an abundant agro-waste. Pomegranate peel extract-mediated SnO_2-TiO_2 nanocomposites exhibited quasi-spherical nanoparticles with a reduced band gap of 2.8 eV and achieved 97.56% degradation of Alizarin Red dye, while maintaining excellent stability over repeated reuse cycles (Sumathi *et al.* 2026). In addition, pomegranate-derived bioactive compounds have been successfully incorporated into electrospun multilayer films, significantly improving their mechanical strength, antioxidant activity, and barrier properties, thereby demonstrating the high functional potential of pomegranate biomass for sustainable material development (Valizadeh *et al.* 2024).

Numerous green-synthesized nanomaterials have demonstrated excellent photocatalytic and adsorption performance toward textile dyes. Senna alexandrina-mediated silver nanoparticles achieved approximately 94% degradation of Reactive Orange 16 and exhibited strong antibacterial activity against both Gram-positive and Gram-negative bacteria (Sangameshwaran *et al.* 2024). Hydrothermally synthesized CuO@A-TiO_2/Ro-TiO_2 nanocomposites completely degraded 100 mg L^{-1} Reactive Orange 16 under both UV and sunlight irradiation (Nassar *et al.* 2024). For comparison, *Solanum nigrum*-mediated CuO nanoparticles achieved 99.1% RO16 removal through adsorption; however, this represents surface uptake rather than oxidative photocatalytic degradation and is therefore considered a distinct treatment mechanism (Murugeshwari *et al.* 2026).

Although considerable progress has been made in developing advanced photocatalysts, experimental optimization of synthesis parameters and degradation conditions remains labor-intensive, time-consuming, and expensive due to the large number of interacting variables. Recently, artificial intelligence and machine learning (ML) have emerged as powerful tools for modelling complex chemical processes, reducing experimental efforts, and improving predictive accuracy. Artificial neural network (ANN) models have successfully predicted methylene blue degradation using green-synthesized TiO_2 nanoparticles prepared from *Cinnamomum tamala* leaf extract with excellent accuracy. More directly relevant studies have applied ML to photocatalytic and nanocatalyst-assisted pollutant degradation. ANN successfully predicted dye degradation using green-synthesized TiO_2 photocatalysts

(Mukherjee *et al.* 2026), while ML-based approaches have also been employed for modelling pollutant degradation using green catalysts. Further integrated phyto-mediated nanomaterials, azo-dye photodegradation, and ML modelling, demonstrating the relevance of data-driven prediction to photocatalytic wastewater treatment (Lin *et al.* 2022). GPR was selected as the principal predictive approach because its kernel-based covariance structure is well suited to smooth nonlinear relationships in relatively small continuous datasets while also providing probabilistic prediction and uncertainty estimates. In comparison, SVR provides effective nonlinear regression without native probabilistic uncertainty estimates, MLP-ANN generally benefits from larger independent datasets, and tree-based ensembles can be less suitable for smoothly varying response surfaces. In the present framework, RSM was employed to design the 27-run Box–Behnken experiment, quantify individual and interaction effects, and identify optimum operating conditions. GPR was subsequently used as a separate nonlinear predictive model based on the same four process variables, providing complementary prediction and uncertainty information rather than independent experimental validation. Thus, RSM provides statistically interpretable process optimization, whereas GPR provides flexible data-driven prediction. Similarly, machine learning has been employed to elucidate catalyst restructuring during CO_2 hydrogenation via in situ STEM analysis, revealing critical catalyst-support interactions that underlie improved catalytic performance (Eliasson *et al.* 2025). Apple peel-mediated PdPtCo nanoparticles, combined with ANN, accurately predicted hydrogen production while simultaneously exhibiting efficient degradation of methylene blue (Altuner *et al.* 2022). Statistical optimization methods, such as Response Surface Methodology (RSM), have also demonstrated effectiveness in optimizing adsorption processes for heavy metal removal (Sugumar *et al.* 2024).

The novelty of this study lies in the integrated development of a pomegranate-peel-mediated Mo-modified TiO_2 photocatalyst for visible-light degradation of Reactive Orange 16 (RO16), coupled with statistical optimization and machine-learning-based prediction. Unlike previous studies that have generally addressed green photocatalyst synthesis, RO16 degradation, process optimization, or predictive modelling independently, the present work combines these elements within a single experimental framework. A four-factor, 27-run Box–Behnken design was employed to quantify and optimize the effects of pH, catalyst dosage, initial dye concentration, and irradiation time, while multiple nonlinear regression models were comparatively evaluated for predictive performance. In particular, Gaussian Process Regression was further examined through cross-validation, uncertainty-oriented prediction, and permutation-based feature interpretation. This combined material–process–modelling strategy provides a reproducible and data-driven approach for improving visible-light photocatalytic treatment of dye-contaminated wastewater.

2. MATERIALS AND METHODOLOGY

2.1 Materials

Pomegranate peel used to synthesize TiO_2 and Mo-doped TiO_2 was obtained from a local fruit shop in Erode, Tamil Nadu, India.

2.2 Green Synthesis of Photocatalysts

Pomegranate peels were thoroughly washed with distilled water to remove dust and impurities, air-dried under ambient conditions, and ground into a fine powder. About 10 g of the powdered pomegranate peel was mixed with 60 mL of deionized water and transferred into a Teflon-lined stainless-steel autoclave. Hydrothermal extraction was carried out at 180 °C for 6 h to obtain a phytochemical-rich extract (Dathan *et al.* 2025). After hydrothermal extraction, the autoclave was allowed to cool naturally to room temperature (approximately 25 ± 2 °C). The recovered extract volume was approximately 50 mL. The extract was filtered through Whatman No. 1 filter paper (nominal pore size approximately 11 µm) to remove insoluble residues. The resulting filtrate was transferred to a sealed amber glass container, stored at 4 °C, and used for photocatalyst synthesis within 24 h of extraction.

For the green synthesis of Mo-modified TiO_2 nanoparticles, 1.0 g of titanium (IV) isopropoxide (TTIP, ≥97% purity) was used as the titanium precursor, while ammonium heptamolybdate tetrahydrate ($(NH_4)_6Mo_7O_{24}\cdot 4H_2O$, ≥99% purity) was used as the Mo precursor. The required amount of the Mo precursor was added along with TTIP to 20 mL of the prepared pomegranate peel extract under continuous magnetic stirring. The reaction mixture was stirred for approximately 30 min to ensure homogeneous mixing of precursors with the phytochemical constituents present in the extract (Jiang *et al.* 2022). Subsequently, the pH of the reaction mixture was adjusted to 9 by dropwise addition of approximately 5 mL of 0.1 M NaOH solution (≥98% purity) under continuous magnetic stirring, with the pH monitored using a calibrated digital pH meter. The phytochemical constituents of the pomegranate peel extract acted primarily as a complexing and stabilizing medium during precursor hydrolysis and nanoparticle formation, assisting particle-growth control and limiting excessive agglomeration.

Following adjustment to pH 9, the reaction mixture was continuously stirred for approximately 2 h to allow precursor precipitation. Completion of precipitation was considered to have been reached when no further visible increase in precipitate formation

occurred during continued stirring. The resulting precipitate was separated by filtration and washed three times with approximately 30 mL of distilled water per cycle, followed by two washing cycles with approximately 20 mL of ethanol per cycle, to remove residual precursor species and organic compounds. The purified precipitate was dried in a hot-air oven at 120 °C for 3 h to remove physically adsorbed moisture and volatile components (Al-Madanat, 2026). Approximately 2.0 g of the dried precursor was placed in an alumina crucible and calcined in a laboratory muffle furnace under an air atmosphere. The temperature was increased from room temperature to 400 °C at a heating rate of 5 °C min^{-1} and maintained at 400 °C for 3 h. After calcination, the furnace was switched off, and the sample was allowed to cool naturally to room temperature inside the furnace (Leela *et al.* 2025). The resulting Mo-modified TiO_2 photocatalyst was collected, finely ground, and stored in an airtight container for subsequent characterization.

For comparison, pristine TiO_2 was synthesized using the same experimental procedure and processing conditions as the Mo-modified TiO_2 photocatalyst, except that ammonium heptamolybdate tetrahydrate was omitted. Briefly, 1.0 g of TTIP was added to 20 mL of the prepared pomegranate peel extract under continuous magnetic stirring. The reaction mixture was stirred for approximately 30 min, followed by adjustment to pH 9 using 0.1 M NaOH solution. The precipitation, filtration, washing, drying at 120 °C for 3 h, and calcination at 400 °C for 3 h were performed under the same conditions described for the Mo-modified sample. The resulting pristine TiO_2 was collected, finely ground, and stored in an airtight container for comparative characterization.

2.3 Characterization Study

Elemental composition of the green-prepared TiO_2 and Mo-modified TiO_2 photocatalysts was determined using EDX coupled with a Gemini Zeiss system. The resulting spectra were examined to verify the presence of titanium, oxygen, and molybdenum in the synthesized materials. Surface functional groups associated with the pomegranate-peel extract and the metal-oxide photocatalysts were investigated by attenuated-total-reflectance Fourier-transform infrared spectroscopy using a PerkinElmer Spectrum Two instrument. Photoluminescence measurements were performed using an Edinburgh Instruments FLS920 spectrometer at an excitation wavelength of 325 nm, and the emission spectra were recorded over the range of 350–650 nm at room temperature. Identical instrumental settings were maintained for pristine TiO_2 and Mo-modified TiO_2 to enable qualitative comparison of their PL intensities. Lower PL intensity was cautiously interpreted as an indication of reduced radiative electron–hole recombination rather than direct evidence of enhanced charge-carrier lifetime. Thermogravimetric analysis (TGA) was performed using a Shimadzu TGA-51 thermogravimetric analyser. Approximately 10 mg of the sample was placed in an alumina crucible and heated from 30 to 900 °C at a heating rate of 10 °C min^{-1} under a continuous nitrogen flow of 50 mL min^{-1}.

2.4 Box–Behnken Experimental Design

The photocatalyst dosage was varied from 15 to 75 mg L^{-1} (equivalent to 0.015–0.075 g L^{-1}). These values represent the mass of photocatalyst added per unit volume of RO16 solution and were maintained consistently throughout the experimental design. A four-factor, three-level Box–Behnken design was employed to investigate the effects of pH, catalyst dosage, initial RO16 concentration, and irradiation time on RO16 degradation efficiency. For four factors ($k = 4$), the Box–Behnken design comprised $2k(k - 1) = 24$ design points. Three additional runs were performed at the design centre to estimate pure experimental error and assess repeatability, resulting in a total of 27 experimental runs. The experimental run order was randomized to minimize potential systematic bias associated with uncontrolled temporal or experimental variations. The factors were evaluated at three coded levels (−1, 0, and +1), corresponding to their low, centre, and high values, respectively.

The experimental ranges of the independent variables were selected based on preliminary photocatalytic trials conducted to identify practically relevant operating windows for RO16 degradation. Accordingly, pH was varied from 3 to 11, catalyst dosage from 15 to 75 mg L^{-1}, initial RO16 concentration from 15 to 55 mg L^{-1}, and irradiation time from 10 to 70 min. These ranges were selected to encompass acidic-to-alkaline conditions and sufficiently broad catalyst-loading, dye-concentration, and irradiation-time intervals for evaluating their individual and interactive effects within the BBD framework.

A single fixed composition of the prepared Mo-modified TiO_2 photocatalyst was used throughout all 27 BBD experiments. Mo loading was not included as an independent variable in the Box–Behnken design; therefore, the optimization was restricted to the operating parameters of pH, catalyst dosage, initial RO16 concentration, and irradiation time.

Table 1. Experimental factors used for the optimization of Reactive Orange 16 (RO16) removal

Factor	Parameter	Unit	Low (-1)	Centre (0)	High (+1)
A	pH	–	3	7	11
B	Catalyst dosage	mg L^{-1}	15	45	75
C	Initial RO16 concentration	mg L^{-1}	15	35	55
D	Irradiation time	min	10	40	70

The actual values were converted into coded values using:

$$x_i = \frac{X_i - X_0}{\Delta X_i} \quad \ldots (1)$$

where x_i were coded values, X_i were actual values, X_0 was the centre value, and ΔX_i is the step change.

2.5 Photocatalytic Degradation of RO16

RO16 solutions were prepared at the concentrations specified by the BBD matrix. For each experimental run, 100 mL of RO16 solution was transferred into a 250 mL borosilicate glass reactor, and the solution pH was adjusted to the required value using dilute NaOH or HCl. The prescribed dosage of Mo-modified TiO_2 photocatalyst was added, and the suspension was continuously stirred at 500 rpm using a magnetic stirrer. Before irradiation, the suspension was maintained in the dark for 60 min under continuous stirring to establish adsorption–desorption equilibrium.

Visible-light irradiation was provided using a 500 W xenon lamp positioned approximately 15 cm from the reactor**.** A UV cut-off filter (λ > 420 nm) was used to restrict irradiation predominantly to the visible-light region. The incident light intensity at the reactor surface was maintained at approximately 100 mW cm^{-2}. The reaction temperature was maintained at approximately 25 ± 2 °C using external cooling during irradiation. The irradiation time was varied from 10 to 70 min according to the BBD experimental matrix.

Following irradiation, the photocatalyst was separated from the treated RO16 solution by filtration using Whatman No. 1 filter paper (nominal pore size approximately 11 µm). The clarified filtrate was subsequently analysed using a UV–Vis spectrophotometer at 330 nm to determine the residual RO16 concentration.

RO16 decolorization efficiency was calculated as (Sahith *et al.* 2025):

$$\text{Degradation}(\%) = \frac{C_0 - C_t}{C_0} \times 100 \quad \ldots (2)$$

where C_0 and C_t were initial and residual RO16 concentrations, respectively.

Control experiments were performed under otherwise identical conditions using RO16 under visible-light irradiation without photocatalyst (photolysis control), RO16 with Mo-modified TiO_2 maintained in darkness (adsorption control), and RO16 with pristine TiO_2 under visible-light irradiation (reference photocatalyst control). All photocatalytic experiments were independently performed in triplicate (n = 3), and the results were expressed as mean ± standard deviation.

2.6 GC–MS Analysis of Degradation Intermediates

Following the photocatalytic degradation of RO16 under the selected experimental conditions, the treated solution was collected, and the suspended photocatalyst was separated by filtration. The resulting clarified solution was subsequently subjected to GC–MS analysis to investigate the degradation intermediates formed during photocatalytic treatment.

2.7 RSM and Statistical Analysis

A second-order polynomial model fitted the degradation response:

$$Y = \beta_0 + \sum_{i=1}^{4} \beta_i x_i + \sum_{i=1}^{4} \beta_{ii} x_i^2 + \sum_{i=1}^{3} \sum_{j=i+1}^{4} \beta_{ij} x_i x_j + \varepsilon \quad \ldots (3)$$

where Y represents the predicted degradation efficiency; $\beta_0, \beta_i,$ βii, and β_{ij} denote the intercept, interaction coefficients, and linear and quadratic terms; and ε shows residual error. Model adequacy was evaluated using ANOVA, R^2, adjusted R^2, predicted R^2, adequate precision, and lack-of-fit.

2.8 Numerical Optimization and Confirmation

Numerical desirability optimization was employed to maximize RO16 degradation while keeping the four operating variables within their experimental limits (Yamini and Devi, 2023). The selected optimum condition was validated using three confirmation trials. Prediction error was calculated as:

$$\text{Error}(\%) = \frac{|Y_{\text{exp}} - Y_{\text{pred}}|}{Y_{\text{pred}}} \times 100 \quad \ldots (4)$$

where Y_{exp} and Y_{pred} represent the confirmation and RSM-predicted responses, respectively.

2.9 ML Dataset and Preprocessing

The ML dataset contained four inputs-pH, catalyst dosage, initial RO16 concentration, and irradiation time- and RO16 degradation efficiency as the output. For preliminary computational modelling, the original BBD dataset was expanded to 120 observations. Missing and non-finite observations were removed before an 80:20 training-testing division. The input variables were standardized by the mean and standard deviation of the training data (Kumar *et al.* 2026):

$$X_{ij}^* = \frac{X_{ij} - \mu_{j,\,\text{train}}}{\sigma_{j,\,\text{train}}} \quad \ldots (5)$$

The same training parameters were applied to the test data to prevent information leakage. Data

preprocessing was performed after partitioning the modelling dataset. The mean and standard deviation used for standardization were estimated exclusively from the training data and subsequently applied unchanged to the test data. Thus, no information from the test subset was used during feature scaling, model fitting, or hyperparameter optimization.

2.10 ML Model Development

Five regression models-Gaussian Process Regression (GPR), Support Vector Regression (SVR), Gradient Boosting, multilayer perceptron artificial neural network (MLP-ANN), and Bagged Random Trees-were developed in MATLAB (Bakır *et al.* 2025). Five-fold cross-validation was performed exclusively within the training dataset for model development and hyperparameter optimization. The held-out test subset was excluded from cross-validation and hyperparameter selection and was used only for final predictive evaluation.

The predictive performance of the developed regression models was evaluated using the coefficient of determination (R^2) (Gaddala *et al.* 2025), mean squared error (MSE), root mean squared error (RMSE), and mean absolute error (MAE), as expressed in Eqs. (6)–(9):

$$R^2 = 1 - \frac{\sum_{i=1}^{n} (y_i - \hat{y}_i)^2}{\sum_{i=1}^{n} (y_i - \bar{y})^2} \quad \ldots (6)$$

$$MSE = \frac{1}{n}\sum_{i=1}^{n} (y_i - \hat{y}_i)^2 \quad \ldots (7)$$

$$RMSE = \sqrt{\frac{1}{n}\sum_{i=1}^{n} (y_i - \hat{y}_i)^2} \quad \ldots (8)$$

$$MAE = \frac{1}{n}\sum_{i=1}^{n} |y_i - \hat{y}_i| \quad \ldots (9)$$

where $y_i, \hat{y}_i, \overleftarrow{\ }$ y, and n denote the measured value, predicted value, mean measured value, and number of observations, respectively. The final model was selected based on its overall performance across R^2, RMSE, MAE, and MSE, together with cross-validation consistency and held-out predictive performance, rather than relying on a single performance metric. Permutation importance was subsequently applied to determine the relative contribution of each input variable. These algorithms were selected to represent complementary nonlinear regression approaches. GPR provides probabilistic kernel-based modelling, SVR offers robust kernel-based nonlinear regression, MLP-ANN captures complex nonlinear relationships, while Gradient Boosting and Bagged Random Trees provide ensemble tree-based approaches capable of modelling nonlinear interactions without imposing a predefined functional relationship.

3. RESULTS AND DISCUSSION

3.1 Characterization

FTIR shows the inclusion of prominent peaks in Fig. 1.

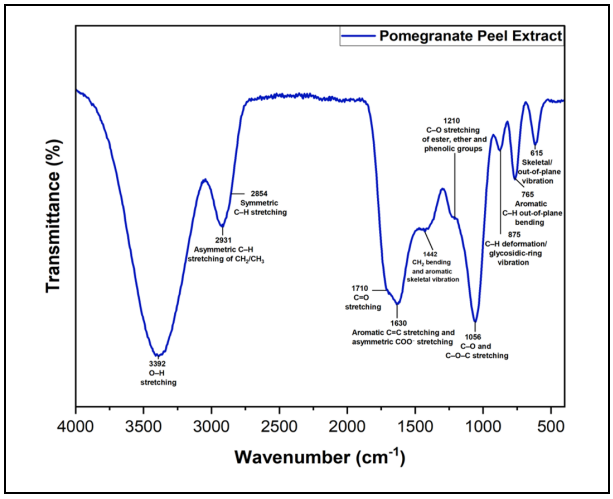

Fig. 1: FTIR of pomegranate-peel extract used for green photocatalyst synthesis

FTIR analysis of the pomegranate-peel extract displayed several absorption bands associated with phytochemical functional groups. The broad band centred at 3392 cm^{-1} was assigned to O–H stretching associated with phenolic compounds, alcohols, and carbohydrates. The absorption band near 2931 cm^{-1} corresponded to aliphatic C–H stretching, while the signal around 1710 cm^{-1} was assigned to C=O stretching associated with carbonyl-containing constituents. The band near 1056 cm^{-1} was attributed to C–O stretching associated with alcohol, ether, and polysaccharide structures. These spectral features indicate the presence of hydroxyl-, carbonyl-, and ether-containing constituents in the pomegranate-peel extract. Because the present FTIR spectrum represents the extract rather than the final TiO_2 or Mo-modified TiO_2 photocatalysts, these observations are used only to characterize the functional groups present in the extract and are not considered direct evidence of phytochemical–nanoparticle interactions, precursor coordination, or surface stabilization. Confirmation of such interactions would require comparative FTIR spectra of the final photocatalysts and additional supporting characterization.

Elemental characterization was subsequently carried out for the undoped TiO_2 and Mo-doped TiO_2 samples using EDX spectroscopy, and the corresponding spectra are presented in Fig. 2(a) and (b). Elemental compositions determined by EDX are presented in Table 2.

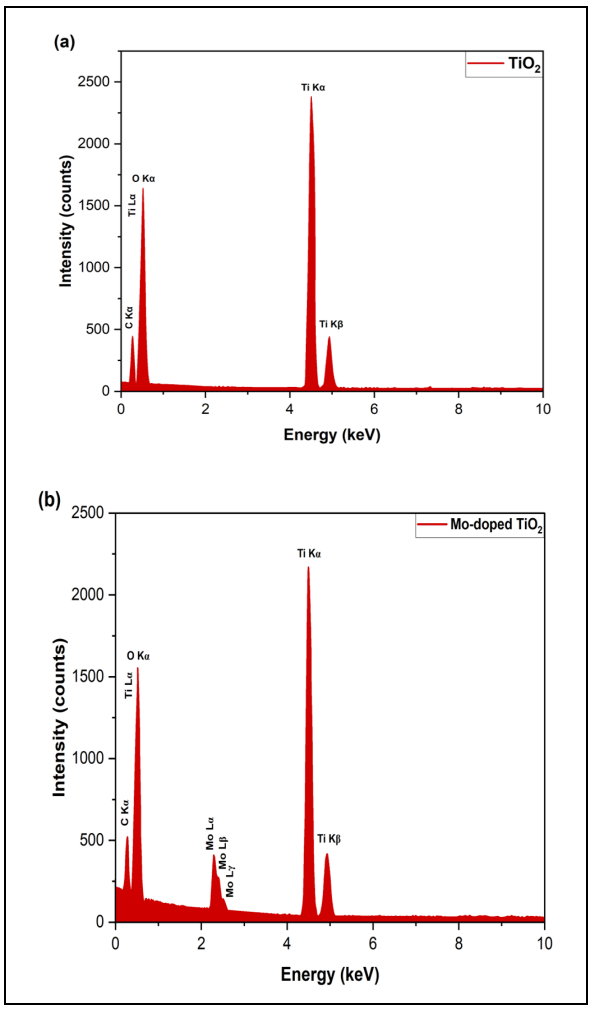

Fig. 2: EDX spectra of the green-synthesized photocatalysts: (a) undoped TiO_2 and (b) Mo-doped TiO_2

Table 2. Elemental composition of synthesized TiO_2 and Mo-doped TiO_2 photocatalysts determined by EDX.

Photocatalyst	Ti (at%)	O (at%)	Mo (at%)
TiO_2	34.20	65.80	–
Mo-doped TiO_2	31.80	63.95	4.25

EDX analysis of the Mo-modified TiO_2 sample revealed the presence of Ti, O, and Mo, with atomic compositions of 31.80, 63.95, and 4.25 at.%, respectively. The measured Mo content of 4.25 at.% represents the elemental composition detected by EDX and should not be directly interpreted as the nominal precursor loading. The nominal Mo content was determined from the relative quantities of the Ti and Mo precursors used during synthesis, whereas the EDX-derived value represents the composition detected within the analysed region of the final photocatalyst. The detectionof Mo confirms its elemental presence in the prepared photocatalyst. However, EDX alone cannot determine whether Mo is substitutionally incorporated into the TiO_2 lattice, deposited on the particle surface, or present as a separate Mo-containing phase. Therefore, the EDX results are interpreted as evidence of Mo presence rather than conclusive proof of lattice-level doping. Further structural and chemical-state analyses, particularly XRD and XPS, would be required to establish the structural location and oxidation state of Mo.

The textural characteristics of the prepared photocatalysts were evaluated using porosity measurements and BET surface area measurements. The resulting mean pore diameter, specific surface area, and total pore volume were summarized in Table 3.

Table 3. Surface area and pore characteristics

Photocatalyst	Average Pore Diameter (nm)	BET Surface Area (m^2/g)	Total Pore Volume (cm^3/g)
TiO_2	8.6	42.8	0.092
Mo doped TiO_2	7.4	61.5	0.114

Introducing Mo increased the specific surface area from 42.8 $m^2\ g^{-1}$ for undoped TiO_2 to 61.5 $m^2\ g^{-1}$ for Mo-doped TiO_2. The doped material also exhibited a greater total pore volume, increasing from 0.092 to 0.114 $cm^3\ g^{-1}$, while its average pore diameter declined slightly from 8.6 to 7.4 nm. The larger surface area and pore volume can provide more accessible adsorption and reaction sites for RO16 molecules, thereby supporting improved photocatalytic activity. The modest reduction in average pore diameter from 8.6 to 7.4 nm indicates a change in the textural characteristics of the Mo-modified TiO_2; however, the underlying particle-growth or structural mechanism cannot be established from BET analysis alone. Comparable improvements in surface-related properties and functional performance were observed following Mo modification of TiO_2 (Jayasawal *et al.* 2022).

The thermal conversion of the pomegranate-peel precursor occurred through several distinguishable stages. The small mass reduction observed below approximately 150 °C was attributed primarily to the elimination of physically adsorbed and bound water. This process corresponded to the broad endothermic DSC

peak centred at approximately 96 °C. Weak DTG features at around 205–220 °C may be associated with volatilization or decomposition of low-molecular-weight extractives and thermally unstable organic constituents.

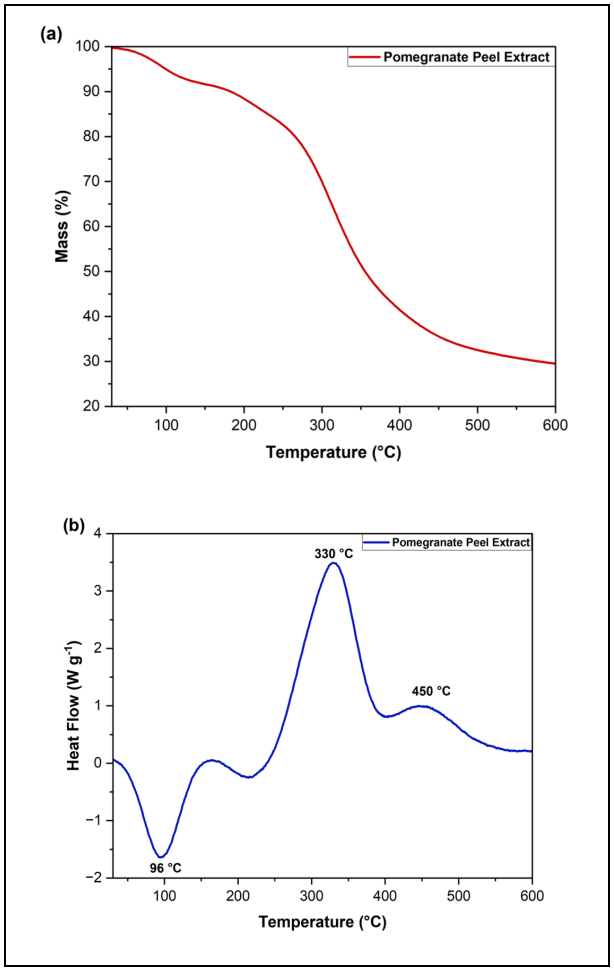

Fig. 3: Thermogravimetric and derivative thermogravimetric profiles of the pomegranate-peel precursor under a nitrogen atmosphere

The most substantial mass change occurred between approximately 250 and 400 °C, corresponding to the decomposition of the principal lignocellulosic components. Hemicellulose generally undergoes thermal breakdown at the lower-temperature end of this interval, producing a comparatively broad derivative signal. Cellulose decomposition occurs over a narrower temperature range and may account for the more pronounced peak observed near 330 °C. In contrast, lignin possesses a heterogeneous, cross-linked aromatic structure and therefore decomposes gradually over a wider temperature range, contributing to the persistent mass reduction above 400 °C.

The thermal event detected at approximately 450 °C may be related to the further thermal decomposition of carbonaceous residues and condensed lignin-derived structures. The small mass change between approximately 500 and 600 °C could arise from the decomposition of thermally stable residual species. However, because no coupled evolved-gas analysis was performed, the identities of gaseous products released during these thermal events were not assigned.

These results demonstrate the multistage thermal decomposition of pomegranate peel arising from its mixture of moisture, extractives, hemicellulose, cellulose, lignin, and mineral constituents. A calcination temperature of 400 °C was employed for the prepared precursor to facilitate thermal removal of residual organic constituents and formation of the oxide material. However, the TGA profile of pomegranate peel was considered only as supplementary information regarding the decomposition of biomass-derived organic constituents and was not assumed to represent the thermal behaviour of the complete Ti/Mo precursor system.

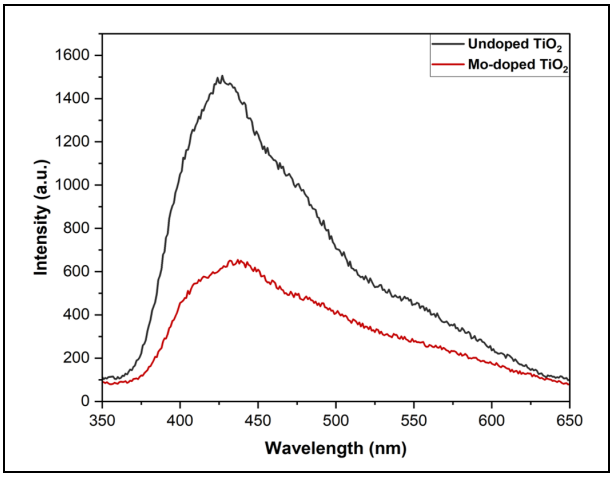

Fig. 4: Photoluminescence spectra of undoped TiO_2 and Mo-doped TiO_2 photocatalysts

The Mo-modified TiO_2 sample exhibited substantially weaker photoluminescence emission than undoped TiO_2. Since PL emission is associated with radiative electron–hole recombination, the reduced PL intensity suggests suppression of radiative recombination in the Mo-modified sample. However, steady-state PL measurements alone cannot directly establish enhanced charge separation or longer charge-carrier lifetime. Therefore, the observed decrease in PL intensity is interpreted cautiously as an indication of reduced radiative recombination, while time-resolved spectroscopic measurements would be required to directly evaluate charge-carrier dynamics and lifetimes.

3.2 Photocatalytic Degradation of Reactive Orange 16

Photocatalytic performance of pomegranate-peel-mediated Mo-doped TiO_2 was evaluated for degradation of Reactive Orange 16 under visible-light

irradiation. Four operating variables solution pH, catalyst dosage, irradiation time, and initial RO16 concentration were investigated using a BBD experimental design. The Mo concentration in the photocatalyst was held constant throughout the experiments to ensure that the observed variations in response were attributable to the selected operating parameters. The experimental conditions and corresponding degradation efficiencies are presented in Table 4.

The RO16 decolourization efficiencies, determined from the decrease in absorbance at 330 nm, ranged from 52.4% to 95.9%, demonstrating the combined influence of the four selected operating variables. The highest decolourization response of 95.9% was obtained at pH 7, an initial RO16 concentration of 15 mg L^{-1}, a catalyst dosage of 45 mg L^{-1}, and an irradiation time of 70 min. Conversely, the lowest decolourization response of 52.4% was observed at pH 11, an RO16 concentration of 35 mg L^{-1}, a catalyst dosage of 15 mg L^{-1}, and an irradiation time of 40 min. Because these values were derived from the decrease in characteristic RO16 absorbance, they represent decolourization and do not by themselves demonstrate complete degradation or mineralization.

Table 4. BBD and RO16 degradation response

Run	pH	Catalyst Dosage (mg L^{-1})	RO16 Concentration (mg L^{-1})	Irradiation Time (Min)	RO16 Degradation (%)
1	7	75	15	40	84.4
2	3	15	35	40	55.5
3	3	45	35	10	58.3
4	7	15	55	40	56.2
5	7	75	55	40	65.6
6	3	45	15	40	78.5
7	7	75	35	70	88.1
8	7	75	35	10	61.7
9	11	75	35	40	61.8
10	7	45	15	70	95.9
11	11	45	55	40	55.5
12	7	45	35	40	82.2
13	11	45	15	40	74.3
14	3	75	35	40	65.9
15	7	45	55	70	81.0
16	3	45	55	40	59.6
17	11	45	35	70	74.1
18	7	45	35	40	81.7
19	7	15	15	40	73.8
20	3	45	35	70	80.4
21	7	45	15	10	78.0
22	7	45	55	10	57.8
23	11	45	35	10	55.9
24	7	15	35	70	72.2
25	11	15	35	40	52.4
26	7	45	35	40	81.9
27	7	15	35	10	57.6

The superior degradation observed under near-neutral conditions can be attributed to favourable interactions between RO16 molecules and the charged surface sites of Mo-doped TiO_2. Solution pH controls the photocatalyst surface charge, dye ionization, and generation of reactive oxygen species. Strongly acidic or alkaline conditions may reduce dye adsorption or modify the availability of hydroxyl and superoxide radicals. Although Ulva lactuca-derived biochar exhibited maximum RO16 adsorption under acidic conditions, the

system involved adsorption rather than photocatalytic oxidation, demonstrating that the optimum pH strongly depends on the treatment mechanism and surface chemistry (Kumar *et al.* 2021).

Increasing the catalyst dosage from its lower level generally improved degradation, as additional photocatalyst increased the number of illuminated active sites and the generation of reactive radicals. Nevertheless, the response exhibited curvature at high catalyst dosages. Excessive suspended particles may scatter incident light, reduce photon penetration, and promote agglomeration. Comparable loading-dependent behaviour has been reported for metal-modified TiO_2 photocatalysts, where an intermediate catalyst concentration provided an appropriate balance between active-site availability and light transmission (Eldoma *et al.* 2024).

An initial RO16 concentration negatively affected degradation efficiency. At low dye concentrations, a greater proportion of RO16 molecules could interact with the available catalytic sites. Increasing dye concentration enhanced competition for these sites and intensified the solution's colour, thereby restricting visible-light penetration. This effect explains the decrease in degradation from 95.9% at 15 mg L^{-1} to 81.0% at 55 mg L^{-1} under otherwise comparable conditions.

Irradiation time exerted a strong positive influence. Longer exposure promoted continuous production of electron–hole pairs and reactive oxygen species, leading to progressive cleavage of the azo linkage and aromatic structure of RO16. For example, at pH 7, a catalyst dosage of 75 mg L^{-1} and an RO16 concentration of 35 mg L^{-1} increased degradation from 61.7% after 10 min to 88.1% after 70 min.

Enhanced activity of Mo-doped TiO_2 was attributed to electronic modification of the TiO_2 lattice. Molybdenum species may introduce localized energy levels and defect sites that trap photogenerated electrons, extend charge-carrier lifetime, and restrict rapid electron–hole recombination. These effects facilitate the formation of hydroxyl and superoxide radicals, which are responsible for dye oxidation. Similar improvements in visible-light activity following transition-metal modification of TiO_2 have been associated with increased charge separation and radical generation (Simović *et al.* 2025).

Overall, the findings demonstrate that pomegranate-peel-mediated Mo-doped TiO_2 can efficiently degrade RO16 under visible-light irradiation. A near-neutral pH, an intermediate catalyst dosage, a low initial dye concentration, and extended irradiation favoured maximum degradation.

3.2.1 Proposed Degradation of RO16

Cleavage of the RO16 azo linkage is expected to generate aromatic intermediates, followed by oxidation of the aromatic rings into lower-molecular-weight compounds. However, decolorization alone does not confirm complete mineralization. Verification of the final products requires total organic carbon analysis, GC–MS analysis, and, where appropriate, toxicity evaluation.

The proposed photocatalytic degradation mechanism of RO16 over Mo-modified TiO_2 involves the photoinduced generation and separation of charge carriers. When the photocatalyst absorbs photons with sufficient energy, electrons are promoted from the valence band to the conduction band, leaving positive holes in the valence band:

$$\mathrm{Mo-TiO_2} + h\nu \rightarrow e^-_{\mathrm{CB}} + h^+_{\mathrm{VB}} \quad \ldots (10)$$

$$\mathrm{O_2} + e^-_{\mathrm{CB}} \rightarrow \mathrm{O_2^{\cdot -}} \quad \ldots (11)$$

$$\mathrm{H_2O} + h^+_{\mathrm{VB}} \rightarrow {}^{\cdot}\mathrm{OH} + \mathrm{H^+} \quad \ldots (12)$$

$$\mathrm{OH^-} + h^+_{\mathrm{VB}} \rightarrow {}^{\cdot}\mathrm{OH} \quad \ldots (13)$$

The generated hydroxyl and superoxide radicals attack the azo bond and aromatic rings of RO16. Successive oxidation produces smaller organic intermediates, which may subsequently undergo mineralization:

$$\mathrm{RO16} + {}^{\cdot}\mathrm{OH} + \mathrm{O_2^{\cdot -}} \rightarrow \text{intermediates} \rightarrow \mathrm{CO_2} + \mathrm{H_2O} + \mathrm{SO_4^{2-}} + \mathrm{NO_3^-} \quad \ldots (14)$$

Mo species associated with the TiO_2 photocatalyst may act as temporary electron-trapping sites, thereby delaying charge recombination and increasing the probability of interfacial redox reactions. The proposed charge-transfer pathway is consistent with the general semiconductor photocatalytic mechanism reported for doped TiO_2 systems (Al-Zamzami *et al.* 2024).

Cleavage of the RO16 azo linkage is expected to generate aromatic intermediates, followed by oxidation of the aromatic rings into lower-molecular-weight compounds. However, decolourization alone does not confirm complete mineralization. Verification of the final products requires total organic carbon analysis, GC–MS analysis and, where appropriate, toxicity evaluation.

3.3 Application of ML to RO16 Degradation Prediction

Machine-learning regression was employed to establish the nonlinear relationship between photocatalytic operating conditions and RO16 degradation efficiency. Four process variables—pH, catalyst dosage, initial irradiation time and RO16

concentration were used as predictors, while degradation efficiency was considered the continuous response. Five regression models were evaluated in MATLAB: Gaussian Process Regression (GPR), Gradient Boosting, Support Vector Regression (SVR), multilayer perceptron artificial neural network (MLP–ANN) and Bagged Random Trees.

3.3.1 ML Dataset Construction

The dataset contained 120 observations distributed across the ranges investigated in the BBD. Each row represented a combination of operating conditions and its associated response; however, only the original 27 BBD observations were experimentally measured, whereas the additional 93 observations were computationally generated for exploratory ML modelling. The additional 93 observations were generated computationally within the experimentally investigated ranges of pH (3–11), catalyst dosage (15–75 mg L^{-1}), initial RO16 concentration (15–55 mg L^{-1}), and irradiation time (10–70 min). Input combinations were generated using a uniform random sampling procedure with a fixed random seed of 42 to ensure reproducibility. The corresponding degradation responses were generated from the fitted second-order RSM polynomial model described in Eq. (3), including its linear, quadratic, and two-factor interaction terms. Thus, the augmented responses represent model-generated estimates rather than independent experimental observations. The augmentation assumes that the fitted RSM response surface provides a reasonable approximation of the experimental process within the investigated factor ranges and that randomly generated combinations within these ranges do not introduce information outside the experimental domain. The 27 experimentally measured observations were retained as the experimental basis, while the 93 generated observations were used only for exploratory computational modelling. Table 5 presents representative observations from the dataset.

Table 5. Representative experimental and computationally generated observations used for exploratory ML modelling

pH	Catalyst Dosage (mg L^{-1})	RO16 Concentration (mg L^{-1})	Irradiation Time (min)	RO16 Degradation (%)
7.00	75.00	15.00	40.00	84.40
3.00	15.00	35.00	40.00	55.50
3.00	45.00	35.00	10.00	58.30
7.00	15.00	55.00	40.00	56.20
7.00	75.00	35.00	70.00	88.10
7.00	45.00	15.00	70.00	95.90
11.00	45.00	55.00	40.00	55.50
5.14	65.55	20.72	49.38	87.30
7.82	52.20	21.48	45.86	89.25
6.76	46.22	15.85	64.63	95.15

Intermediate factor combinations appearing in Table 5, such as pH 5.14 and catalyst dosage 65.55 mg L^{-1}, correspond to computationally generated observations and were not additional experimentally conducted BBD runs.

3.3.2 Data Preprocessing

The dataset was first screened for missing, non-numeric, and non-finite values. All 120 observations satisfied the initial quality criteria and were retained. The three centre-point replicates originating from the original 27-run BBD were preserved because they represented valid experimental replicate responses rather than accidental duplicates. The additional computationally generated observations in the 120-row ML dataset were not considered experimental replicates. The dataset was randomly divided into 80% for training and 20% for testing, corresponding to 96 and 24 observations, respectively. A fixed random seed of 42 was used to ensure reproducibility. Input standardization was performed after data partitioning using only the mean and standard deviation of the training subset (Geetanjali *et al.* 2026):

$$X_{ij}^{*} = \frac{X_{ij} - \mu_{j,\,\text{train}}}{\sigma_{j,\,\text{train}}} \quad \ldots (15)$$

where X_{ij}^{*} is the standardized value, X_{ij} is the original input, and $\mu_{j,\,\text{train}}$ and $\sigma_{j,\,\text{train}}$ are the training-set mean and standard deviation of the jth variable.

3.3.3 Statistical Characteristics and Correlation Analysis

The descriptive statistics of the ML dataset are given in Table 6. The mean values of pH, catalyst dosage, RO16 concentration, and irradiation time were close to their corresponding centre levels, indicating broader numerical sampling across the selected factor ranges. However, the computationally generated observations do not represent additional independent experimental information beyond the original 27 BBD runs.

Table 6. Descriptive statistics of the ML dataset

Variable	Count	Mean	Standard Deviation	Minimum	Maximum
pH	120	7.0024	2.4037	3.00	11.00
Catalyst dosage (mg L^{-1})	120	44.9952	18.0341	15.00	75.00
RO16 concentration (mg L^{-1})	120	35.0053	12.0184	15.00	55.00
Irradiation time (min)	120	40.0108	18.0188	10.00	70.00
RO16 degradation (%)	120	72.3228	10.3598	51.09	95.90

Pearson correlation analysis was performed to investigate the direction and magnitude of linear associations. Irradiation time showed a positive correlation with degradation ($r = 0.5707$) and with catalyst dosage ($r = 0.4021$). The initial RO16 concentration showed a negative correlation ($r = -0.5504$), indicating reduced degradation at higher dye concentrations. The weak pH correlation ($r = -0.0623$) does not imply that pH was unimportant because its effect was predominantly nonlinear, as demonstrated by the significant quadratic term in the RSM analysis.

Table 7. Pearson correlation coefficients with RO16 degradation

Input Variable	Correlation with Degradation
Irradiation time	0.5707
Catalyst dosage	0.4021
Initial RO16 concentration	-0.5504
pH	-0.0623

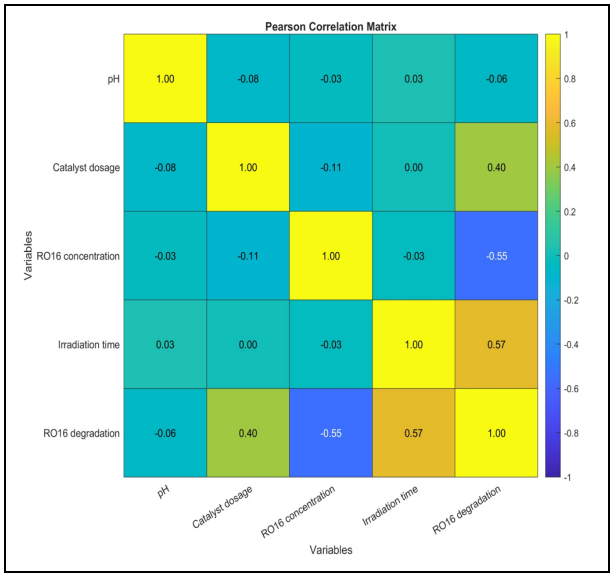

Fig. 5: Pearson correlation heatmap of pH, catalyst dosage, initial RO16 concentration, irradiation time and RO16 degradation efficiency

3.3.4 Model Training and Control of Overfitting

Several measures were adopted to obtain an unbiased assessment of predictive performance. Fivefold cross-validation was used to train the subset during hyperparameter optimization. Bayesian optimization was used instead of GridSearchCV to identify suitable model settings while minimizing unnecessary combinations. The 20% test subset remained excluded from all tuning operations and was used only for final evaluation.

The standardization parameters were estimated exclusively from the training subset. GPR controlled model flexibility through kernel and noise parameters, whereas SVR used kernel scale, box constraint, and epsilon. The learning rate, tree size, and number of learning cycles regulated Gradient Boosting. The MLP–ANN employed two hidden layers and regularization, while bootstrap aggregation was applied in the Bagged Random Trees model. The five models and their principal tuning parameters are summarized in Table 8.

4. MACHINE-LEARNING ANALYSIS

4.1 Comparison of ML Models

The test-set results of the five regression algorithms are summarized in Table 9. Among the evaluated algorithms, GPR exhibited the highest preliminary test-set performance, with an R^2 of 0.99762 and the lowest RMSE, MAE, and MSE, while SVR also showed high predictive performance with an R^2 of 0.99523. Gradient Boosting and MLP-ANN achieved R^2 values close to 0.95, whereas Bagged Random Trees showed comparatively lower test-set performance. These results represent performance within the augmented modelling dataset and should not be interpreted as independent experimental validation. The test-set performance of the five regression models is compared in Table 9, while the corresponding R^2 values are displayed in Fig. 7. The GPR model was subsequently evaluated using the final validation procedure described in Section 4.2. The GPR performance reported in Table 9 represents the preliminary test-set evaluation obtained during comparison of the five regression algorithms. Following model selection, the GPR model was re-evaluated using the final validation procedure described in Section 4.2, and the resulting values are reported in Table 10.

Therefore, Table 10 provides the definitive performance metrics for the selected GPR model, whereas the values in Table 9 are retained only for comparative screening of the five algorithms.

The strong performance of GPR can be related to its ability to represent smooth nonlinear relationships in relatively small continuous datasets. Its kernel-based covariance structure effectively described the curvature in the response to pH and catalyst dosage while also capturing the monotonic effects of irradiation time and initial dye concentration. SVR produced a similarly strong result because its kernel formulation permitted nonlinear mapping while controlling model complexity.

Table 8. ML models and principal tuning parameters

Model	Principal Parameters
GPR	kernel scale, Kernel function, basis function, and noise level
SVR	kernel scale, Kernel function, box constraint, and epsilon
Gradient Boosting	Learning cycles, learning rate, leaf size, and maximum splits
MLP–ANN	Architecture 4–12–6–1, ReLU activation and regularization
Bagged Random Trees	Learning cycles, leaf size, maximum splits and sampled predictors

Table 9. Test-set performance of the five regression models

Rank	Model	R^2	RMSE	MAE	MSE
1	Gaussian Process Regression	0.99762	0.44264	0.32655	0.19593
2	Support Vector Regression	0.99523	0.62593	0.50317	0.39179
3	Gradient Boosting	0.94891	2.04960	1.69520	4.20080
4	MLP-ANN	0.94686	2.09030	1.63620	4.36940
5	Bagged Random Trees	0.77546	4.29670	3.52740	18.46100

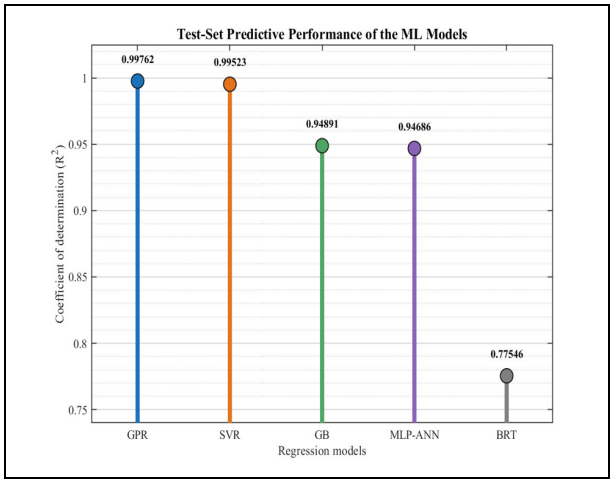

Fig. 7: Comparison of test-set R^2 values obtained using the five regression models

Gradient Boosting and MLP–ANN produced acceptable predictions but showed greater errors than GPR and SVR. The 120-observation dataset may not have provided sufficient independent information for the neural network to fully exploit its flexible architecture. Bagged Random Trees generated the lowest R^2, indicating that piecewise tree partitions were less suitable for the smooth response surface represented by the dataset.

4.2 Cross-validation and Internal Validation of GPR

The selected GPR model was further evaluated using five-fold cross-validation within the available modelling dataset. This procedure provides internal computational validation and should not be interpreted as independent experimental validation. It obtained a test R^2 of 0.99390, with RMSE, MAE, and MSE values of 0.70846, 0.49569, and 0.50192. Five-fold cross-validation produced an $R^2$of 0.99098. The difference between the test and cross-validated R^2 values was only 0.00292, indicating similar performance across these internal validation procedures. The test-set and five-fold cross-validation results of the selected GPR model are provided in Table 10. Its actual-versus-predicted and residual plots are shown in Fig. 8(a) and (b).

Table 10. Final performance of the selected GPR model on the test set and five-fold cross-validation

Metric	Test Set	Five-fold Cross-validation
R^2	0.99390	0.99098
RMSE	0.70846	1.00669
MAE	0.49569	0.78071
MSE	0.50192	1.01343

The slightly larger cross-validation errors are expected because every fold uses a smaller training subset. Nevertheless, both R^2 values exceeded 0.99, indicating a close fit within the available augmented dataset. However, these results should not be interpreted as evidence of external predictive capability because the underlying experimental basis comprised only 27 BBD runs. The close distribution of predicted and actual observations around the equality line further indicates good agreement within the evaluated modelling dataset.

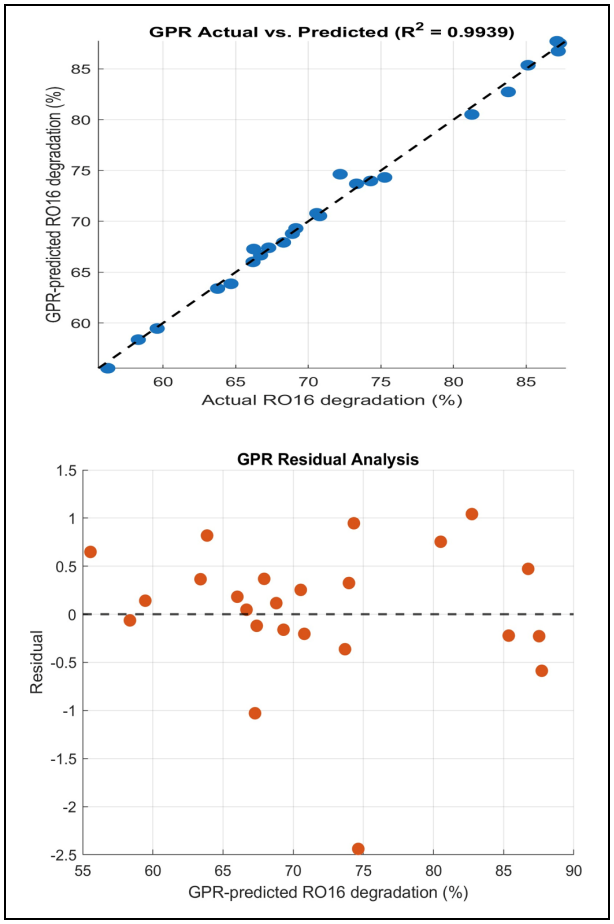

Fig. 8: Diagnostic performance of the selected GPR model: (a) actual versus predicted degradation efficiencies and (b) residual distribution

Predicted values were closely distributed around the equality line, while residuals remained randomly scattered around zero. The small difference between the test and cross-validated R^2 values indicated stable model generalization.

4.3 Residual Behaviour

The GPR residuals remained closely clustered around zero without an obvious systematic upward or downward trend, indicating no pronounced systematic pattern in the evaluated predictions. However, visual inspection of the residual distribution alone does not establish residual normality or homoscedasticity, which would require additional formal diagnostic testing. The MAE of 0.49569 indicates a relatively low average absolute prediction deviation within the evaluated augmented dataset. Similarly, the low RMSE indicates that large prediction deviations were comparatively limited. Nevertheless, these error metrics should be interpreted cautiously because the augmented dataset contains computationally generated observations and therefore do not establish independent experimental predictive reliability.

4.4 Prediction Under Optimized Conditions

The optimal conditions identified by RSM were subsequently evaluated using the developed GPR model to compare the numerical predictions of the two modelling approaches. At pH 7.07, an initial RO16 concentration of 17.75 mg L^{-1}, a catalyst dosage of 50.40 mg L^{-1}, and an irradiation time of 68.12 min, GPR predicted a response of 96.3121%, whereas the corresponding RSM prediction was 96.2701%, resulting in a numerical difference of 0.0420 percentage points. This close numerical agreement indicates consistency between the two modelling approaches within the present computational framework; however, it should not be interpreted as independent validation because the GPR analysis was not based on a separate experimental dataset.

The GPR prediction was also close to the experimental confirmation response of 95.88%, with an error of 0.4507%. The model-derived 95% prediction interval at the optimum ranged from 94.4382% to 98.1860% and encompassed both the RSM prediction and the confirmation response. However, this interval represents model-based uncertainty within the present GPR framework and should not be considered a comprehensive assessment of uncertainty or independent experimental validation. The responses predicted by RSM and GPR are compared with the experimental confirmation response in Table 11 and Fig. 9.

Table 11. RSM, GPR and confirmation comparison

Item	Value
Optimum pH	7.07
Optimum catalyst dosage	50.40 mg L^{-1}
Optimum RO16 concentration	17.75 mg L^{-1}
Optimum irradiation time	68.12 min
RSM prediction	96.2701%
GPR prediction	96.3121%
Confirmation response	95.8800%
GPR–RSM difference	0.0420 percentage points
GPR confirmation error	0.4507%
GPR 95% prediction interval	94.4382–98.1860%

The close agreement demonstrates that RSM and GPR captured a comparable relationship between the operating variables and the degradation of RO16. RSM provided an interpretable quadratic representation of the individual and interaction effects, whereas GPR offered flexible nonlinear prediction together with uncertainty estimation. As shown in Fig. 9, GPR predicted a degradation efficiency of 96.31%, closely agreeing with the RSM prediction of 96.27% and the confirmation response of 95.88%. The GPR and RSM predictions differed by only 0.042 percentage points, demonstrating strong consistency between the two modelling approaches

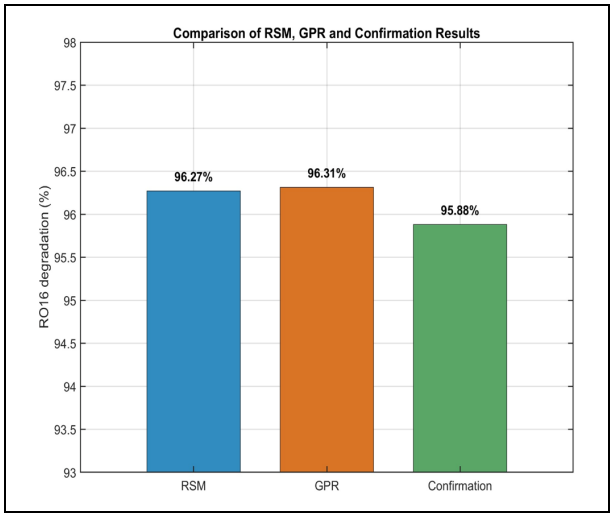

Fig. 9: Comparison of RO16 degradation efficiencies predicted by RSM and GPR with the confirmation response under optimized operating conditions

GPR differed from the RSM prediction by only 0.042 percentage points and produced a confirmation error of 0.4507%. This close numerical agreement indicates consistency between the statistical and machine-learning approaches within the present modelling framework but does not constitute independent model validation.

4.5 Importance of the Photocatalytic Variables

Permutation importance was evaluated on the held-out test subset by independently permuting each input variable while keeping the remaining variables unchanged and quantifying the resulting reduction in GPR predictive performance. The resulting raw importance scores were normalized by dividing each feature importance by the sum of the importance scores of all four predictors and multiplying by 100, such that the normalized importance values summed to 100%. Within the developed GPR model and the evaluated dataset, initial RO16 concentration exhibited the highest normalized permutation importance (34.188%), followed by catalyst dosage (23.588%), irradiation time (23.079%), and pH (19.145%). The permutation importance of the four GPR input variables is reported in Table 12 and illustrated in Fig. 10.

Table 12. GPR permutation importance

Rank	Input Variable	Importance (%)
1	Initial RO16 concentration	34.188
2	Catalyst dosage	23.588
3	Irradiation time	23.079
4	pH	19.145

The comparatively high importance assigned to RO16 concentration may be associated with its effects on light attenuation, active-site competition, and the number of pollutant molecules available for oxidation. Similarly, catalyst dosage may influence the availability of illuminated reaction sites, whereas irradiation time determines the duration of photocatalytic treatment. Although pH exhibited the lowest permutation importance within the GPR model, its nonlinear contribution was also considered through the RSM analysis.

The GPR permutation-importance ranking differed slightly from the Pearson correlation and RSM ANOVA results because these approaches quantify different aspects of the input–response relationship. Pearson correlation describes pairwise linear association, permutation importance quantifies the dependence of GPR predictive performance on each input variable, whereas RSM ANOVA evaluates the statistical significance of linear, interaction, and quadratic terms within the fitted response-surface model. Therefore, the rankings obtained from these methods should not be interpreted as directly equivalent measures of factor influence.

The initial RO16 concentration was identified as the most influential predictor, followed by catalyst dosage, irradiation time, and pH. This ranking represents the contribution of each variable to GPR prediction rather than its isolated statistical effect.

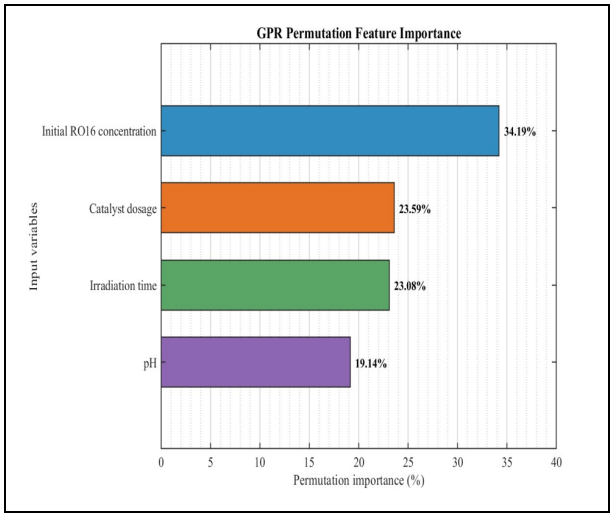

Fig. 10: Permutation-based importance of the four input variables in the selected GPR model

4.6 Integration of RSM and GPR

The combined RSM–GPR framework provided complementary information for evaluating the photocatalytic process. The BBD–RSM stage reduced the number of required factor combinations and quantified linear, interaction, and quadratic effects. Numerical desirability optimization subsequently identified the operating conditions associated with the maximum predicted response. In contrast, GPR provided a flexible nonlinear modelling approach for exploring the input–response relationship within the available augmented dataset.

The difference of 0.0420 percentage points between the RSM and GPR predictions indicates close numerical agreement within the present modelling framework; however, this agreement does not constitute independent validation or by itself demonstrate a substantial methodological advantage. The complementary framework combines the statistical interpretability and experimental-design capability of RSM with the flexible nonlinear predictive capability of GPR. GPR also provided a model-based 95% prediction interval at the identified optimum; however, this represents a limited assessment of predictive uncertainty rather than comprehensive uncertainty quantification. Thus, the combined approach may provide complementary statistical and data-driven information for exploratory optimization of photocatalytic wastewater-treatment processes.

5. CONCLUSIONS

Pomegranate-peel-mediated Mo-doped TiO_2 demonstrated promising potential for the visible-light degradation of Reactive Orange 16. The BBD effectively quantified the effects of pH, catalyst dosage, initial dye concentration, and irradiation time while reducing the number of required factor combinations. The quadratic RSM model exhibited strong statistical adequacy, with an R^2 of 0.9996, an adjusted R^2 of 0.9992, and a predicted R^2 of 0.9979, together with a statistically significant model and nonsignificant lack-of-fit, consistent with the ANOVA results.

The RSM-derived optimum conditions were a pH of 7.07, a catalyst dosage of 50.40 mg L^{-1}, an RO16 concentration of 17.75 mg L^{-1}, and an irradiation time of 68.12 min. Under these conditions, RSM predicted 96.27% RO16 decolorization, compared with an experimental confirmation response of 95.88%, corresponding to a prediction error of approximately 0.40%. Among the five evaluated regression algorithms, GPR exhibited the strongest predictive performance within the present augmented modelling dataset, achieving a test R^2 of 0.99390 and a cross-validated R^2 of 0.99098. However, these metrics represent internal computational performance and should not be interpreted as independent experimental validation. The GPR prediction of 96.31% showed close numerical agreement with the RSM prediction; however, this agreement was not interpreted as independent model validation.

Within the developed GPR model and evaluated dataset, permutation-importance analysis identified initial RO16 concentration as the highest-ranked predictor, followed by catalyst dosage, irradiation time, and pH. Overall, the combined RSM–GPR approach provided complementary statistical and data-driven information for exploratory optimization of the photocatalytic treatment process. Future work should validate the expanded modelling dataset using independent experiments and evaluate mineralization, intermediate toxicity, catalyst recyclability, and performance in actual textile wastewater.

FUNDING

This research received no specific grant from any funding agency in the public, commercial, or not-for-profit sectors.

CONFLICTS OF INTEREST

The authors declare that there is no conflict of interest.

COPYRIGHT

This article is an open-access article distributed under the terms and conditions of the Creative Commons Attribution (CC BY) license (http://creativecommons.org/licenses/by/4.0/).

REFERENCES

Abedi, K., Shahmoradi, B., Mohammadi, E., Wantala, K., Maleki, A., Zandsalimi, Y., Salimi, S. and Kohzadi, S., Photocatalytic degradation of VOCs from air stream using Mo: TiO_2/GAC nanocomposites, *Mater. Res. Exp.*, 9(2), 025502 (2022). https://doi.org/10.1088/2053-1591/ac4aa3

Al-Madanat, O. Y., From Organic Waste to Clean Fuel and Water: Plant-Extract-Assisted TiO_2 Nanoparticles for Simultaneous 2-Naphthol Degradation and H_2 Production, *Nanoenergy Adv.*, 6(2), 18 (2026). https://doi.org/10.3390/nanoenergyadv6020018

Altuner, E. E., El Houda Tiri, R. N., Aygun, A., Gulbagca, F., Sen, F., Iranbakhsh, A., Karimi, F., Vasseghian, Y. and Dragoi, E. N., Hydrogen production and photocatalytic activities from $NaBH_4$ using trimetallic biogenic PdPtCo nanoparticles: Development of machine learning model, *Chem. Eng. Res. Des.*, 184, 180–190 (2022). https://doi.org/10.1016/j.cherd.2022.05.021

Al-Zamzami, M., Al-Gheethi, A., Alzaeemi, S. A., Al-Sahari, M., Al-Maqtari, Q. and Noman, E., Validity of zinc oxide nanoparticles biosynthesized in food wastes extract in treating real samples of printing ink wastewater; prediction models using feed-forward neural network (FFNN), *Chemosphere*, 362, 142793 (2024). https://doi.org/10.1016/j.chemosphere.2024.142793

Bakır, R., Orak, C. and Horoz, S., Enhancing photocatalytic degradation of hazardous pollutants with green-synthesized catalysts: A machine learning approach, *J. Environ. Manage.*, 385, 125695 (2025). https://doi.org/10.1016/j.jenvman.2025.125695

Dathan, P. C., Nallaswamy, D., Rajeshkumar, S., Nair, A. R., Deepthy, S. S., Revathy, C. V., Ismail, S., Joseph, S., Jocob, J. and Jose, L., In vitro Evaluation of Anti-inflammatory, Antioxidant Activity of Pomegranate Peel Extract Mediated Calcium Sulphate, Titanium Dioxide Nano Composite, *Trends Biomater. Artif. Organs*, 39(1), 15–24 (2025). https://doi.org/10.5281/zenodo.16792816

Eldoma, M. A., Alaswad, S. O., Mahmoud, M. A., Qudsieh, I. Y., Hassan, M., Bakather, O. Y., Elawadi, G. A., Abouatiaa, A. F. F., Alomar, M. S., Elhassan, M. S., Alhindawy, I. G. and Ahmed, Z. M., Enhancing photocatalytic performance of Co-TiO_2 and Mo-TiO_2-based catalysts through defect engineering and doping: A study on the degradation of organic pollutants under UV light, *J. Photochem. Photobiol. A: Chem.*, 446, 115164 (2024). https://doi.org/10.1016/j.jphotochem.2023.115164

Eliasson, H., Chiang, Y. T., Araújo, T. P., Li, X., Erni, R., Mitchell, S. and Pérez-Ramírez, J., Tracking Dynamics of Supported Indium Oxide Catalysts in CO_2 Hydrogenation to Methanol by In situ TEM, *Adv. Mater.*, 37(20), 2419859 (2025). https://doi.org/10.1002/adma.202419859

Gaddala, B., Devi, K. V., Balakrishnan, V., Sundramurthy, V. P., Hariprabhu, M., Mayakannan, S., Kadaikunnan, S. and Khaled, J. M., Evaluation of detoxification performance of Pithecellobium dulce seed pod powder upon acid treatment: removal of reactive red 195-A dye and kinetic analysis, *Zeitschrift für Physikalische Chemie*, 239(6), 885–910 (2025). https://doi.org/10.1515/zpch-2024-0879

Geetanjali, R., Sreehari, T. M., Vignesh, V., Bodade, V., Parameswari, D. and Anand, J., Machine Learning-assisted Optimization of TiO_2/CuO Nanocomposites for Enhanced Energy Storage Performance, *J. Environ. Nanotechnol.*, 15(2), 401–417 (2026). https://doi.org/10.13074/jent.2026.06.2622190

Golka, K., Kopps, S. and Myslak, Z. W., Carcinogenicity of azo colorants: Influence of solubility and bioavailability, *Toxicol. Lett.*, 151(1), 203–210 (2004). https://doi.org/10.1016/j.toxlet.2003.11.016

Jayasawal, A., Sharma, S., Singh, S. and Srivastava, P., Extensive enhancement in power conversion efficiency of dye-sensitized solar cell by using Mo-doped TiO_2 photoanode, *J. Sol. State Electrochem.*, 26(10), 2209–2217 (2022). https://doi.org/10.1007/s10008-022-05238-3

Jiang, L., Wang, F., Xie, C., Xie, X., Meng, X. and Zhang, H., High-Amylose Corn Starch/Konjac Glucomannan Composite Films Incorporating Nano TiO_2 and Pomegranate Peel Extract and Their Application as Coatings on Agaricus bisporus, *J. Polym. Environ.*, 30(11), 4550–4561 (2022). https://doi.org/10.1007/s10924-022-02498-y

Kumar, A., Poornima, S. N., Subbulakshmi, R., Selvaraju, M., Raj, K. G. and Jayabalan, C., Hierarchical green carbon fibers from banana pseudostem for efficient Pb^{2+} adsorption: Kinetics, isotherms, and machine learning prediction, *Interact.*, 247(1), 188 (2026). https://doi.org/10.1007/s10751-026-02534-6

Kumar, M., Sujatha, S., Gokulan, R., Vijayakumar, A., Praveen, S. and Elayaraja, S., Prediction of RSM and ANN in the decolorization of reactive orange 16 using biochar derived from ULVA Lactuca, *Desalin. Water Treat.*, 211, 304–318 (2021). https://doi.org/10.5004/dwt.2021.26615

Leela N, S., Kannan, S., Abisheik, T., Tiffany, M., Pandiyan, V., Periyasami, G., Barmavatu, P., Shanmugaraj, K. and Balu, K., Enhanced photocatalytic activity of azo dyes degradation by urea assisted Mo-doped TiO_2 under UV-A light and sunlight irradiation, *J. Alloys Compds.*, 1020, 179389 (2025). https://doi.org/10.1016/j.jallcom.2025.179389

Li, G., Mang, C., Xing, L., Cao, P., Cai, Y., Luo, J. and Jiang, H., Surfactant-assisted synthesis of Mo-doped TiO_2/FAC (fly ash cenosphere) for degradation of methylene blue dye under visible light irradiation, *Colloids Surf. A: Physicochem. Eng. Aspects*, 651, 129669 (2022). https://doi.org/10.1016/j.colsurfa.2022.129669

Lin, J., Gulbagca, F., Aygun, A., Elhouda Tiri, R. N., Xia, C., Van Le, Q., Gur, T., Sen, F. and Vasseghian, Y., Phyto-mediated synthesis of nanoparticles and their applications on hydrogen generation on $NaBH_4$, biological activities and photodegradation on azo dyes: Development of machine learning model, *Food Chem. Toxicol.*, 163, 112972 (2022). https://doi.org/10.1016/j.fct.2022.112972

Mukherjee, C., Chaudhuri, M. G., Modak, N. and Biswas, D., A Machine Learning Approach to Predict Dye Degradation Efficiency Using ANN in Photocatalytic Systems, *J. Water Environ. Nanotechnol.*, 11, 96–112 (2026). https://doi.org/10.22090/jwent.2026.2082125.2042

Murugeshwari, S., Gunasekaran, M., Rathi, B. S., Saravana, K. R. M. and Divya, J., Plant-Mediated CuO Nanoparticles for Reactive Orange Dye Adsorption: Experimental study and Machine Learning-Assisted Optimization, *Water, Air Soil Pollut.,* 237(16), 945 (2026). https://doi.org/10.1007/s11270-026-09615-w

Nassar, A. A., Elfiky, A. A. E. A., El-Sawaf, A. K. and Mubarak, M. F., Sustainable green synthesis and characterization of nanocomposites for synergistic photocatalytic degradation of Reactive Orange 16 in textile wastewater using CuO@A-TiO_2/Ro-TiO_2, *Sci. Rep.*, 14(1), 16188 (2024). https://doi.org/10.1038/s41598-024-63294-3

Ravichandran, K., Suvathi, S., Ayyanar, M., Kavitha, P. and Praseetha, P. K., Vermiwash-mediated synthesis of molybdenum doped TiO_2 nanoparticles: Evaluation of photocatalytic and biomedical properties, *J. Photochem. Photobio. A: Chem.*, 446, 115169 (2024). https://doi.org/10.1016/j.jphotochem.2023.115169

Sahith, V. N., Kumar, J. A., Rose, R. L., Anbarasan, P., Gomathi, S. and Sruthi, V. S., Fabrication of Activated Carbon-HKUST-1 MOF Nanocomposites for Enhanced Adsorption and Decontamination of Acidic and Basic Dyes in Wastewater, *J. Environ. Nanotechnol.*, 14(4), 192–208 (2025). https://doi.org/10.13074/jent.2025.12.2541842

Sangameshwaran, V., Ragu Prasath, A., Selvam, K., Obaidullah, A. J., Kumar Yadav, K. and Sudhakar, C., Green synthesis of silver nanoparticles using Senna alexandrina leaf extracts and their antibacterial, larvicidal, nanotoxicity and photocatalytic activity, *Inorganica Chimica Acta*, 571, 122220 (2024). https://doi.org/10.1016/j.ica.2024.122220

Setiye, A., Xu, Q., Feng, G., Yan, X., Wang, C., Song, C. and Lu, H., Synthesis of Mo-doped TiO_2 nanostructure by hydrothermal method for enhancing TEA gas sensing performance, *J. Alloys Compds.*, 1036, 182149 (2025). https://doi.org/10.1016/j.jallcom.2025.182149

Simović, B., Radovanović, Ž., Dikić, J., Milojković, N., Gasik, M., Branković, G. and Dapčević, A., Multifunctional reusable Ag-decorated ZnO nanostructured photocatalyst obtained by green synthesis, *Ceram. Int.*, 51(19), 27269–27281 (2025). https://doi.org/10.1016/j.ceramint.2025.03.402

Sugumar, M., Bharathi, S., Sampath, V., Sundramurthy, V. P., Selvaraju, M., Kadaikunnan, S. and Khaled, J. M., Biosorption of Pb(II) ions through nanostructured teff straw based magnetized activated biocarbon: Aspects on modeling, optimization, and kinetics, *Global Nest J.,* 26(9), (2024). https://doi.org/10.30955/GNJ.06479

Sumathi, A., Kamatchi, T., Maruthavanan, T. and Epshiba, R., Green synthesis of SnO_2–TiO_2 nanocomposite using pomegranate peel extract for efficient photocatalytic degradation of Alizarin Red dye, *Chem. Pap.*, (2026). https://doi.org/10.1007/s11696-026-05144-2

Valizadeh, R., Zandi, M., Ganjloo, A. and Dardmeh, N., Bioactive multilayer film based on the sage seed gum-gelatin, TiO_2 and electrospun zein fibers encapsulating pomegranate peel extract, *Int. J. Biol. Macromol.*, 283, 137826 (2024). https://doi.org/10.1016/j.ijbiomac.2024.137826

Yamini, V. and Devi, R. V., Effective Bio-mediated Nanoparticles for Bioremediation of Toxic Metal Ions from Wastewater – A Review, *J. Environ. Nanotechnol.*, 12(2), 12–33 (2023). https://doi.org/10.13074/jent.2023.06.232467